# Design of High-Power Ultra-High-Speed Rotor for Portable Mechanical Antenna Drives

Md Khurshedul Islam, *Student Member, IEEE*, Seungdeog Choi, *Senior Member, IEEE* Yang-Ki Hong, and Sangshin Kwak, *Member, IEEE* 

Abstract—This paper presents the design of high-power ultra-high-speed (HP-UHS) rotors of permanent magnet machines for a mechanical-based ULF-VLF antenna (AMEBA) application. The conventional communication system in an RF-denied environment (e.g., underground and under seawater facilities) is power demanding with very low efficiency and low power density. Thus, a portable communication system was not available until recently. Such a critical limitation could be overcome by utilizing an HP-UHS motor as a mechanical communication transmitter. This is a first attempt to the best of authors' knowledge. However, the unprecedentedly high-speed and high-power AMEBA exhibit new design challenges, including the critical mechanical resonance of the rotor, coupled with wireless communication bandwidth (ULF-VLF). It limits the highest possible efficiency and power density of portable AMEBA systems while achieving a required design safety margin (DSM). In this paper, such critical constraints of HP-UHS rotors are analytically derived and integrated into a design model. This new design model will effectively couple the electromagnetic, thermal, structural, and rotordynamic analysis for the successful AMEBA rotor design. In the optimization, the kriging method is adopted to create the efficient approximation model of the design nonlinearities. Multiple objectives and Pareto-front analysis are used to obtain an efficient rotor design with high DSM. The proposed approach is applied to design a 2 kW 500 000 r/min rotor considering AMEBA requirements. The effectiveness of the rotor for the AMEBA application has been validated through 3-D FEA and experimental testing.

Index Terms—Finite element analysis (FEA), Multiphysics analysis, mechanical antenna, multi-objective optimization, rotordynamic, structural integrity, and ultra high speed.

Manuscript received February, 25, 2021; revised April, 19, 2021, and October, 29, 2021, and accepted December, 03, 2021. Date of current version December, 10, 2021. This work was supported in part by the NSF CCSS-Comms Circuits and Sens System Program (Award # 1905434). (Corresponding author: Seungdeog Choi and Sangshin Kwak)

Md Khurshedul Islam and Seungdeog Choi are with Department of Electrical and Computer Engineering at the Mississippi State University, Starkville, MS 39759, USA (e-mail: mi264@msstate.edu, seungdeog@ece.msstate.edu).

Yang-Ki Hong is with the Department of Electrical and Computer Engineering at the University of Alabama, Tuscaloosa, AL, USA. (e-mail: ykhong@eng.ua.edu)

Sangshin Kwak is with the Chung-Ang University, Seoul, South Korea. (e-mail: sskwak@cau.ac.kr)

#### I. INTRODUCTION

IN RECENT years ultra-high-speed machines (UHSM) are ■getting more attention in high-tech industries such as robotics, spindle, portable charger, aerospace, and medical applications [1]-[3]. Apart from these, one of the new emerging applications of the UHSM is the wireless communication system using ultra-very low frequency (ULF-VLF: 0.3-10 kHz) in the RF-denied environment [4]. Wireless communication in such a harsh environment is limited in distance, efficiency, and portability because of the conventional coil antenna's gigantic size and excessive input current requirement [5]. One of the most promising solutions to this problem is to use a mechanicalbased antenna (AMEBA) by utilizing a UHSM, as shown in Fig. 1. Our previous work presents the usefulness and fundamental operations of the AMEBA system using a motor drive [6]. Unlike conventional coil antenna, the AMEBA uses a UHSM to rotate a polarized permanent magnet (PPM) dipole for generating the alternating magnetic field with no additional power consumption. Therefore, the AMEBA solves the power requirement problem and drastically reduces the antenna size. Consequently, it makes the antenna portable, enabling bidirectional wireless communication between the earth's surface and underground or underwater facilities. Also, using the rareearth magnet as a PPM dipole significantly improves the antenna's field generation efficiency. For example, let us compare a mechanical antenna using a cylindrical Nd-Fe-B (G-N52, Length = Radius = 10 cm) magnet with an N-turn coil loop electric antenna of the same cross-sectional area. To obtain an equivalent field, the electrical coil antenna requires a large DC current of  $\sim 10^5/N$  A, whereas the static magnet consumes no current. This simple example shows the benefit of AMEBA.

However, one of the critical challenges in AMEBA system development is designing its mechanical transmitter i.e., the ultra-high-speed (UHS) rotor to drive the PPM dipole at ULF-VLF. First, operating a rotor in this frequency range will encounter several critical bending frequencies (CBFs). Usually, the UHS rotor does not operate at or close to its CBFs to avoid mechanical resonance [7]-[8]. However, the AMEBA rotor cannot afford this flexibility because it will limit the antenna's communication bandwidth. Secondly, the AMEBA rotor requires a high shaft torque at UHS to rotate the high mass density PPM. This high-power requirement pushes the rotor design parameters to a sensitive threshold considering the structural strength limit of the rotor materials. An insufficient design safety margin (DSM) will lead the antenna to structural breakdown. Finally, considering the AMEBA's portability, the UHSM must have high efficiency and compact cooling system.

Fig. 1. Simplified illustration of the AMEBA system using an HP-UHSM.

The AMEBA motor requires an operating speed of ~500 000 r/min or more. However, there are limited design approaches in this range. The first 500 000 r/min 100 W permanent magnet synchronous machine (PMSM) was reported in 2005 [9]. The rotor was designed using a total loss minimizing optimization. Although the optimization did not include multi-physics influences, the temperature and stress of the rotor were well below the material limit due to the low shaft-torque design. A 1000 000 r/min 100 W and 330 000 r/min 1 kW UHSM for turbo compressor systems are presented in [10], but the detailed analysis on the rotor design, structural integrity, and rotordynamics has been limited. A 500 000 r/min 100 W PMSM using multi-physics design algorithm is presented in [11]. The rotor is designed separately, and a specific air-friction loss directly constraints its parameter. Besides PM machines, the switched reluctance machine has also been studied for lowpower UHS operation in [12]. The rotor has a rated speed of 1200 000 r/min and is designed using a cohesive zone model to limit the rotor stress. It has three CBFs below the rated speed.

All of these UHS rotors are designed for very low shaft torque at the rated speed (1.9 mNm [9], [11], and 0.79 mNm [12]) while the AMEBA rotor requires much higher torque with additional design constraints. In addition, these design models have to be further studied to design a high-power UHS (HP-UHS) rotor by considering the following issues.

First, the CBF has to be integrated into design constraints in rotor geometry optimization, along with the air-friction loss and centrifugal stress. Since the HP-UHS rotor tends to require a high L/D ratio to increase the rotor's torque density, the rotor's CBF could be below the rated frequency, which might result in dangerous mechanical resonance during AMEBA operation.

Second, the mutual influence of multi-physics performances has to be considered in geometry optimizations. For example, the temperature of the HP-UHS rotor changes severely as the air -friction loss change with geometry variation. This temperature change significantly influences PM material's electromagnetic property and rotor stress development, resulting in electromechanical performance degradation. Considering the AMEBA system will be utilized in safety-critical applications, such multiphysics analysis with additional AMEBA constraints is critical.

Third, multiple objectives have to be utilized to optimize the HP-UHSM for portable AMEBA with many system parameters, such as the communication bandwidth, transient time, and PPM dipole inertia. Simultaneously achieving the high efficiency and high DSM of the AMEBA rotor is extremely challenging due to the mutual influence of multi-disciplinary constraints. A design point with the highest efficiency can commonly result in excessive centrifugal stress or PM temperature in the HP-UHS rotor, which is not acceptable in safety-critical AMEBA applications.

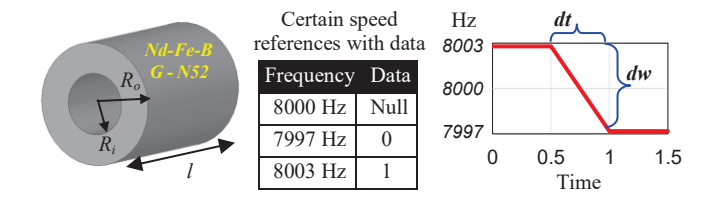


Fig. 2. PPM dipole geometry and example of AMEBA rotor dynamic.

This paper presents a new design approach of HP-UHSM using multi-physics and multi-objective optimization for the AMEBA system, especially a 2 kW 500 000 r/min rotor. The optimized UHSM is prototyped, and its key requirements for the AMEBA system are validated using FEA and experimental testing. Considering the UHS rotor design is the most critical part of the HP-UHSM development in AMEBA application, this article provides an in-depth analysis of the HP-UHS rotor design, including its impact on the overall efficiency and DSM.

The rest of the paper is organized as follows. Section II presents the derivation of rotor specifications from AMEBA requirements. Section III presents the critical design constraints of HP-UHS rotors. Section IV describes the proposed multiphysics design method. Section V shows the design of 2 kW 500 000 r/min AMEBA rotor. The FEA simulation and experimental validation of the AMEBA rotor are presented in sections VI and VII. Finally, section VIII concludes the paper.

#### II. DERIVATION OF UHS AMEBA ROTOR SPECIFICATIONS

The design specifications of the HP-UHSM are derived from the AMEBA system requirements. In our previous AMEBA design [4], a 12 W 10 000 r/min motor drive has been used with a PPM dipole of  $1.83\times10^{-6}$  kgm². Due to the limited power and speed rating of motor drive, the antenna has a maximum data transfer rate (DTR) of 2 Hz/s with a bandwidth of 88-116 Hz. It is capable of transmitting only ~7 characters per minute in a distance of few meters. In this studied design, the antenna is aimed to transmit more than 50 characters per minute beyond 1 km distance and increase the bandwidth up to 8.3 kHz. To achieve this, the AMEBA system requires 8333 Hz frequency (f) and a PPM of  $1.1\times10^2$  Am² magnetic dipole moment (m). The magnetic field from this rotating dipole can be found as:

$$\overrightarrow{B_{dip_{rot}}} = \frac{_{3\mu_0 \, m}}{_{8\pi r^3}} \sum_{k \in \{x, y, z\}} a_k \cos(\omega_m t) + b_k \sin(\omega_m t) ] \hat{k} \quad (1)$$

where  $\omega_m$  corresponds to the rotating frequency of the dipole. For  $\omega_m = 8333$  Hz and the minimum pole number (p = 2), the required motor speed can be calculated by  $N_r = 120 f / p$ . Considering a hollow cylinder PPM to generate the required m, the total motor inertia can be calculated as:

$$J_L = J_r + J_s + J_d \approx J_d \approx \frac{1}{2} \pi \rho (R_o^2 - R_i^2) (R_o^2 + R_i^2) l$$
 (2)

where  $J_r$ ,  $J_s$  and  $J_d$  are the rotor, shaft, and dipole inertia;  $\rho$ ,  $R_o$ ,  $R_i$ , and l are the density and PPM dipole dimensions, as shown in Fig. 2. In this design,  $J_d = 1.62 \times 10^{-4} \text{ kgm}^2 \gg (J_r + J_s)$ . Fig. 2 also shows the dynamic of AMEBA rotor for communication operation, which requires a frequency change of 6 Hz with 0.5s transient, i.e., a DTR of 12 Hz/s. Considering this rotor dynamic,

the required motor power can be calculated by:

$$P = \frac{2\pi}{60} S_F \underbrace{\left(\tau_l + J_L \frac{d\omega_m}{dt}\right)}_{T_o} \times N_r \tag{3}$$

where  $S_F$  is a safety factor,  $\frac{d\omega_m}{dt}$  is the DTR, and  $\tau_l$  is the load torque. Furthermore, for the safety-critical AMEBA application, a multi-physics DSM is required and the machine should have at least the state-of-the-art UHSM efficiency. Based on these considerations, the UHSM specifications are summarized as:

- $\sim$ 38 mNm shaft torque at 500 000 r/min ( $\approx$  2 kW UHSM).
- No critical bending frequency of the rotor below 8333 Hz.
- At least 30% multi-physics DSM and 94% efficiency.

# III. CRITICAL DESIGN CONSTRAINTS OF UHS AMEBA ROTOR

# A. Basic Rotor Geometry and Material Selection

For UHS over 100 000 r/min, a 2-pole rotor is preferred to minimize the core loss and switching loss. Two potential UHS rotor topologies are shown in Fig. 3. Type-1 has a steel shaft at the rotor center, and a retaining sleeve is used to protect the PM from scattering. This topology is mechanically rigid and easy to build. However, it limits the PM usage in the rotor, reducing the rotor's torque density considerably. Therefore, it is not preferred for AMEBA rotors that requires high power density for portable application. For the AMEBA rotor, type-2 topology is selected, where the shaft is removed from the rotor center to maximize PM usage, resulting in a high torque density of the rotor.

The potential application of AMEBA is small unmanned vehicles in underground and undersea, which primarily operate with limited energy storage. Thus, it is unlikely that liquid or active cooling is available. Also, there is a possibility to use a vacuum system to remove the air-friction loss, which makes it further challenging for heat removal. Considering such factors, the maximum rotor temperature is allowed 150° C, and at least 94% efficiency is targeted, which is  $\sim$ 5 % more than state of the art [9]. Based on these requirements, rear earth magnet Nd-Fe-B and  $Sm_2Co_{17}$  are two candidates to use as PM material. Nd-Fe-B is mechanically stronger and has higher  $B_r$ , but it has an operating temperature of only 80°C, which limits its use in the AMEBA rotor. Hence  $Sm_2Co_{17}$  is the preferred option for AMEBA rotors; it can work up to 350° C. The sleeve material should be mechanically strong and lightweight. Some suitable candidates are titanium alloy, steel, Inconel alloy, and carbon fiber [8]-[11]. However, these materials have different physical and thermal properties; hence their multi-physics influence must be evaluated. To do that, the material optimization is coupled with the machine sizing in the proposed design method.

# B. Air-friction Loss

The air-friction loss is one of the major limiting factors of designing an AMEBA rotor. According to the scaling law [13], the shaft power of the UHS rotor can be increased by enlarging the outer rotor radius ( $R_2$ ). However, increasing  $R_2$  of AMEBA rotor results in an exponential rise of the air-friction loss. At UHS operation, this loss becomes significant, even a dominant part of the machine's overall loss, which reduces the machine efficiency drastically. It also affects the rotor's axial temperature distribution, which may lead the PM to uneven magnetization,

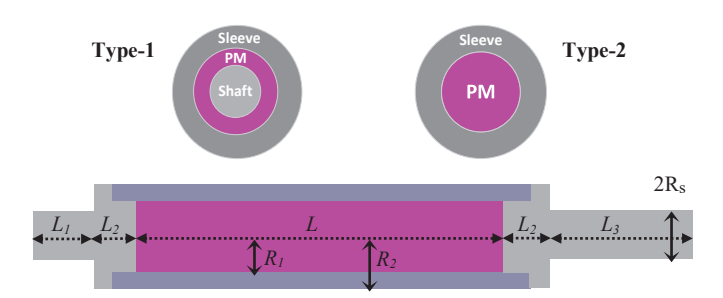


Fig. 3. UHS rotor configurations and axial cross-section of type-2 rotor.

resulting in vibration of the AMEBA rotor by increasing the torque ripple. Therefore, in the AMEBA rotor optimization, this loss must be calculated accurately and consider its impact on both the electromagnetic and thermal performance. The air-friction loss of the type-2 rotor can be calculated using (4):

$$P_f = \pi C_r C_d \rho_{air} \omega^3 R_2^4 l_r \tag{4}$$

where  $C_r$  is the rotor surface roughness coefficient,  $l_r$  is the rotor axial length exposed to the air-gap,  $\omega$  is the rotational speed, and  $\rho_{air}$  is the air density.  $C_d$  is the drag coefficient, depends on the rotor geometry and airflow behavior. In [9]-[12],  $C_d$  is estimated by analytical equation  $C_d \propto Ta^{-0.2}$ , where  $T_a$  is the Taylor number. However, for the AMEBA rotor, accurate calculation of  $C_d$  is highly recommended because it is directly proportional to air-friction loss. In the proposed design model, the computational fluid dynamic (CFD) analysis is used to calculate the  $C_d$  accurately. In CFD,  $C_d$  can be defined as:

$$C_d = \frac{Shear\ stress\ on\ rotor\ surface}{Dynamic\ Pressure} = \int (\omega_r, R_2, l_r, l_a, C_r) \ (5)$$

When the air-gap length  $(l_a)$  and rated speed  $(\omega_r)$  are fixed in the optimization, the  $C_d$  can be pre-calculated using parametric CFD analysis for different values of  $R_2$  and  $l_r$ , which can be used as a 2-D look-up table in the air-friction loss model of (4).

# C. Critical Bending Frequency

As the air-friction-loss is proportional to the 4<sup>th</sup> power of the outer rotor radius, a sizeable stack length (L) needs to be used in the AMEBA rotor to obtain high shaft torque. However, increasing L results in several CBFs of the AMEBA rotor below its rated frequency [14]. Operating an AMEBA rotor close to CBF will lead the antenna to mechanical vibration, which can directly affect its transmitting signal profile. Hence, the CBF calculation must be included in the AMEBA rotor optimization to restrict it above the rated frequency with a separation margin ( $C_{SM}$ ) as:

$$\omega_{n^{th} CBF} > C_{SM} \cdot \omega_m$$
 where  $n = 1, 2, \dots$  (6)

At the design stage, accurate calculation of CBF is difficult because it is highly manipulated by the rotor's guide-bearing stiffness and its installation process. Therefore, in the proposed design method, the rotor's undamped natural frequency (UNF) is used as an indicator of actual CBF. This consideration is rational because the actual CBF will be higher than the UNF due to the bearing damping. An analytical model is developed using the Rayleigh-Ritz method [15] to calculate the UNF of the AMEBA

rotor. The simplified UNF equation can be written as:

$$\omega_n = \sqrt{\frac{(1/512)a_n^2 (E_{SL} + E_{PM}) R_2^4}{\left[\rho_{SL} \left\{R_S^2 L_1^4 + R_S^2 L_3^4 + 2R_2^2 L_2^4 + (R_2 - R_1)^2 L^4\right\} + \rho_{PM} R_1^2 L^4\right]}}$$
(7)

where  $\omega_n$  is the  $n_{th}$  UNF of the rotor,  $R_1$  is the PM radius,  $R_s$  is the shaft radius,  $L_1$ ,  $L_2$ , and  $L_3$  are shaft lengths as shown in Fig. 3,  $E_{SL}$ ,  $E_{PM}$ ,  $\rho_{SL}$ , and  $\rho_{PM}$  are the Young Modulus and mass density of the sleeve and PM material,  $a_n$  is a series constant of  $n_{th}$  UNF, depends on the rotor's boundary conditions.

# D. PM Temperature

In the HP-UHS rotor, the PM experiences a high operating temperature due to the excessive air-friction loss. This temperature rise reduces the PM's maximum energy product  $((BH)_{max})$ , which directly affects the torque performance and control parameters of the AMEBA motor. Since AMEBA communication requires a high DTR, the parameter variation due to PM temperature is critical in the AMEBA operation. Furthermore, the PM temperature also affects the AMEBA rotor's radial displacement and stress development significantly by thermal expansion. Therefore, during the AMEBA rotor optimization, the PM temperature must be calculated and evaluated its impact on the electromagnetic and structural performance. To do that, a lumped parameter thermal model (LPTM) of the full motor is developed, as shown in Fig. 4, and integrated into the optimization model. In the LPTM, current sources represent the heat sources generated by corresponding losses. The voltage source represents the ambient temperature. This model considers the convection and conduction heat transfers while the radiation is neglected. The equivalent convective and conductive thermal resistances are calculated using Newton's law of cooling and Fourier's conduction law, respectively. Ten nodal points represent the temperature of the different motor parts. Node  $T_4$  and  $T_6$  are the winding and the PM temperature, which can be transferred to other physics models and constrained as a thermal aspect as (8):

$$T_4 < T_w$$
 (Limited by the coil insulation type)  $T_6 < T_m$  (Considering a desire  $(BH)_{max}$ ) (8)

#### E. Retaining Sleeve Thickness

A retaining sleeve is used in the UHS rotor to protect the rotating PM against its centrifugal force. Also, increasing the sleeve thickness  $(t_{SL})$  reduces the rotor stress considerably. However, a thick sleeve increases the effective airgap length, which reduces the AMEBA rotor's torque density. Also, it increases the air-friction loss exponentially and inversely affects the CBF of the AMEBA rotor. As a result, the loss-minimizing optimization algorithms always search for the smallest sleeve thickness value. But, the AMEBA rotor, which uses a large PM, requires enough sleeve thickness to hold the PM; otherwise, the fragile PM will break down and scatter at UHS operation. To avoid this situation, the sleeve thickness for each design point is restricted above the minimum required sleeve thickness  $(t_{SL,min})$  in the AMEBA rotor optimization. For the type-2 rotor topology, the  $t_{SL,min}$  is calculated by (9):

$$t_{SL,min} = \frac{c_{SF}\rho_{SL}\omega^{2}(R_{1}+R_{2})R_{1}^{2}}{64\sigma_{f_{SL}}}$$
(9)

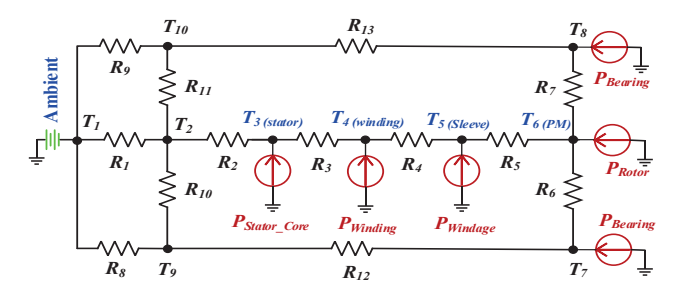


Fig. 4. Simplified lumped parameter thermal model of HP-UHSM.

where  $C_{SF}$  is the mechanical safety factor and  $\sigma_{f_{SL}}$  is the flow tensile stress of sleeve material. According to (9), the  $t_{SL,min}$  is proportional to the third power of  $R_1$ . In practice, the  $t_{SL}$  can also be constrained by the manufacturing ability [10]. In that case, the minimum thickness limit should be included in (9).

# F. Static Interference Fit Length

The interference-fitting is used between the sleeve and PM to secure their rigid assembly with a positive contact pressure  $(P_c)$  to ensure proper torque transfer from the PM to rotor shaft. The applied static interference fit length (SIFL) is calculated by  $\Delta \delta_o = (R_{pm_o} - R_{sl_i})$ , where  $R_{pm_o}$  is the outer PM radius and  $R_{sl_i}$  is the inner sleeve radius. For a low torque UHS rotor, the required SIFL is  $\sim 2$  to 7.5  $\mu$ m, which is easy to implement [9]-[12]. Whereas, the required SIFL for the AMEBA rotor increases exponentially as the PM radius increases, making the rotor assembly difficult. However, the maximum possible SIFL for a specific rotor geometry and material is practically limited by the material's allowable temperature  $(T_{SL} \& T_{PM})$ , coefficient of thermal expansion (CTE)  $(\alpha_{th})$ , and the PM radius  $(R_1)$  as:

$$\Delta \delta_{o,max} = \alpha_{th} R_1 (T_{sleeve} - T_{PM}) \tag{10}$$

Hence, the SILF of AMEBA rotors must be less than  $\Delta\delta_{o,max}$ . Also, it should be selected such that the  $P_c$  at UHS remains positive and the developed stress on both the PM and sleeve remains below their material's strength limit considering a desire DSM. In the proposed design method, a structural analytical model is developed using the static equilibrium theory [16], which integrates the thermal effect and interference fit effect with the rotor displacement and stress variation as (11) and (12):

$$u_{i}(r) = \frac{1}{E_{i}} \left( k_{1,i} r (1 - v_{i}) - k_{2,i} \frac{1}{r} (1 + v_{i}) - \frac{1 - v_{i}^{2}}{8} \rho_{i} r^{3} \omega^{2} \right) + \alpha_{th,i} r \left( T_{max,i} - T_{o} \right)$$

$$\sigma_{r,i}(r) = k_{1,i} + k_{2,i} \frac{1}{r} - \frac{3 + v_{i}}{8} \rho_{i} r^{2} \omega^{2}$$

$$\sigma_{t_{i}}(r) = k_{1,i} - k_{2,i} \frac{1}{r^{2}} - \frac{1 + 3v_{i}}{8} \rho_{i} r^{2} \omega^{2}$$

$$(11)$$

$$p_{c} = \frac{E_{m}E_{s}(u_{m} + u_{s} - \Delta\delta_{o})(R_{2}^{2} - R_{1}^{2})}{E_{s}[(R_{1}^{3} - R_{1}R_{2}^{2})\nu_{m} - R_{1}^{3} + R_{1}R_{2}^{2}] + E_{m}[(R_{1}R_{2}^{2} - R_{1}^{3}) + R_{1}^{3} + R_{1}R_{2}^{2}]}$$
(12)

where r is the distance from rotor center; i = PM or sleeve; u is the radial displacement;  $\sigma_t$  and  $\sigma_r$  are the tangential and radial stress,  $T_o = 25^{\circ}$  C,  $T_{max,i}$  is the corresponding material temperature updated from the thermal model. The constants

 $k_{1,PM}$ ,  $k_{2,PM}$ ,  $k_{1,SL}$ , and  $k_{2,SL}$  are calculated using the boundary conditions of the rotor geometry. One of the boundary conditions integrates the SIFL with the stress model as (13). In the optimization,  $\Delta \delta_{o,max}$  is calculated for each design point and apply (13). The contact pressure constraint is applied as (14) to ensure a stable torque transfer at UHS loading operation.

$$u_{SL}(r=R_1) - u_{PM}(r=R_1) = \Delta \delta_o < \Delta \delta_{o,max}$$
 (13)

$$P_c > 0 MPa \quad (0 \le \omega \le \omega_{max}, \ 0 \le T_i \le T_{max,i}) \quad (14)$$

# IV. MULTIPHYSICS DESIGN MODEL

Due to the inter-disciplinary complexity in designing the AMEBA rotor discussed in section III, a multi-physics optimization approach is developed to design an AMEBA motor for ULF-VLF (up to 8.3 kHz) communication. Fig. 5 shows a simplified workflow of the proposed design approach. First, the UHSM specifications are derived from the targeted AMEBA communication requirements as described in section II. Then initial considerations are made based on the AMEBA system requirements and the required power/speed level.

The design model is developed in the ANSYS workbench using both FEA and analytical models. In the high-power density AMEBA rotor design, accurate estimation of electromagnetic performance is crucial, especially the electromagnetic losses for thermal analysis. Hence, an FEA model is used to analyze the electromagnetic losses, current density, average torque, and material saturation by considering the non-linear electromagnetic properties. However, a complete FEA-based multi-physics optimization requires enormous computational power and time. It becomes even worse if multi-physics models are coupled with additional design constraints from AMEBA system and if the optimization model has a higher number of design variables. Therefore, analytical models are developed for the structural, thermal, and rotordynamic analysis to make the proposed optimization model computationally efficient. The parameter-set feature of ANSYS Workbench is used to couple these models with the optimization module.

In the optimization module, the design of experiment (DOE) technique is used to generate initial samples for each input design parameter. The samples are selected such that it covers the entire design space. The design of AMEBA rotor presents several non-linearities due to the multi-disciplinary constraints associated with the AMEBA communication operation and system requirements. These include the sleeve thickness variation with  $R_1$  and  $\omega$ , SIFL variation with  $R_1$ , air-friction-loss variation with  $\omega$  and  $\omega$ , CBF variation with rotor's L/D ratio, stress variation with temperature, and non-linear magnetic behavior of active part materials. The Kriging method is used to create effective approximation models (response surfaces) to address these non-linearities. Kriging is a semi-parametric interpolation method whose response function combines a global model (polynomial) and a stochastic process term as:

$$\mathcal{Y}(x) = f(x) + \mathcal{Z}(x) \tag{15}$$

where  $\mathcal{Y}(x)$  is the response function of interest (unknown) of design parameter x, f(x) is the deterministic function (known)

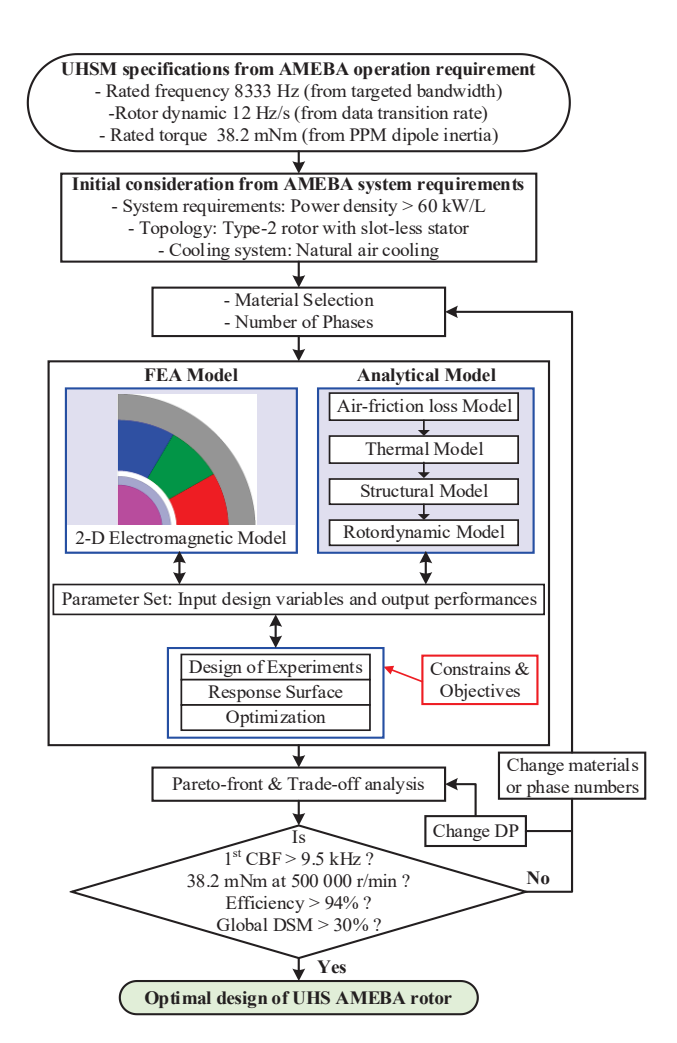


Fig. 5. Proposed multi-physics design approach of UHS AMEBA rotor.

of x, and Z(x) is the error function with zero mean, variance of  $\sigma^2$ , and non-zero covariance matrix  $C_m$ , which is defined by:

$$C_m = Cov[x^i, x^j] = \sigma^2 \mathcal{R}[R_F(x^i, x^j)]$$
  $i, j = 1, 2, \dots, n$  (16)

where  $x^i, x^j$  are the sample points of x from DOE,  $\mathcal{R}$  is the correlation matrix,  $R_F$  is the correlation function, and n is the total sample number of x. The guided initial DOE samples are used to establish the correlation functions. Therefore, the Kriging model can generate efficient approximation models for the high-order local nonlinearities of the electric machine [17]. The approximation models are used in optimization for prediction purposes. The multi-disciplinary constraints and objective functions are defined in the optimization module. For the AMEBA rotor, multiple objectives are used to obtain an efficient design with high DSM. In multi-objective optimization, the optimal solution is a trade-off among all the objectives, hence the pareto-front analysis is used to obtain the best solution.

When the optimization model requests a new design point (DP), the FEA electromagnetic simulation is first solved, and then the analytical models are evaluated sequentially, as shown in Fig. 5. The thermal model uses the electromagnetic and airfriction losses as the input heat source for the corresponding DP. The obtained PM and sleeve temperature are then used in the structural model to consider the rotor's thermal expansion.

The 1<sup>st</sup> UNF of that DP is calculated in the rotordynamic model. Once all the DPs are solved, the Pareto-front can be obtained based on the defined constraints and objectives. Then, the optimal design that satisfies all the AMEBA rotor specifications and has the highest DSM is searched from the Pareto-solutions by an appropriate trade-off. If no DP is found with a desire DSM, change the materials or phase number in the outer loop.

# V. DESIGN OF 2 KW 500 000 R/MIN AMEBA ROTOR

#### A. Initial Consideration

Considering the required power, speed level, and application background, type-2 topology is selected for the AMEBA rotor with a slot-less stator. Fig. 6 shows the 2-D FEA parametric electromagnetic model of full motor used in the optimization. The slot-less stator eliminates the slot harmonics, reducing the torque ripple and rotor eddy current. The shaft lengths ( $L_1$ ,  $L_2$ , and  $L_3$ ) are kept constant on the basis of application requirement and bearing housing. To make the shaft length minimum and avoid additional circuit complexity, UHS ball bearings are considered. The natural air cooling of the motor is used to make the AMEBA system compact and portable. Litz wire is utilized in the slot-less stator to minimize the eddy current effect on the copper loss. The air-gap length is selected as 0.6 mm.

# B. Global Optimization Objectives and Constraints

Three global optimization objectives are considered for the studied AMEBA motor, which are defined as:

$$\begin{cases} OF_1(x) = \text{Seck target of } 38.2 \text{ mNm at } 500\ 000\ r/min \\ OF_2(x) = \text{Minimize } P_E = P_{cu_{dc}} + P_{cu_{ac}} + P_{Fe} + P_{rotor} \\ OF_3(x) = \text{Minimize } P_f \end{cases}$$

The first objective is defined to achieve the 38.2 mNm shaft torque at 500 000 r/min to drive the selected PPM dipole. The other two objectives are to minimize the total electrical loss and air-friction loss separately. The electrical loss consists of copper DC loss, copper proximity loss, stator core loss, and rotor power loss. Besides, nine multi-disciplinary constraints are defined as:

$$S_1(x) = {
m Stator\ peak\ flux\ density\ } (B_{P_{stator}}) < 1.1\ {
m T}$$
  $S_2(x) = {
m Current\ density\ } (J_{den}) < 5\ {
m A/mm}^2$   $S_3(x) = {
m Power\ density\ } (P_{den}) > 60\ {
m kW/L}$   $S_4(x) = {
m Max.\ coil\ temperature\ } (T_{W_-max}) < 130^0\ {
m C}$   $S_5(x) = {
m Max.\ PM\ temperature\ } (T_{PM_-max}) < 150^0\ {
m C}$   $S_6(x) = {
m Max.\ PM\ stress\ } \sigma_{PM} < 100\ {
m MPa}$   $S_7(x) = {
m Max.\ Sleeve\ stress\ } (\sigma_{SL}) < \lambda\sigma_{\rm t,SL}\ {
m MPa}$   $S_8(x) = {
m Contact\ pressure\ } (p_c) > 0\ {
m MPa}$   $S_9(x) = 1^{\rm st\ UNF\ } (\omega_{1st}) > 8500\ {
m Hz}$ 

The electromagnetic constraints  $S_1$ ,  $S_2$ , and  $S_3$  are applied based on the material's saturation limit, air-cooling and the AMEBA system requirement. The thermal constraints  $S_4$  and  $S_5$  are selected based on the desire PM  $(BH)_{max}$  and coil insulation limit. The structural constraints  $S_6$  and  $S_7$  are from the material's physical strength limit considering a minimum safety factor  $(\lambda)$ . The practical constraint  $S_8$  ensures proper torque transfer. The rotor dynamic constraint  $S_9$  restricts the CBFs above 8333 Hz.

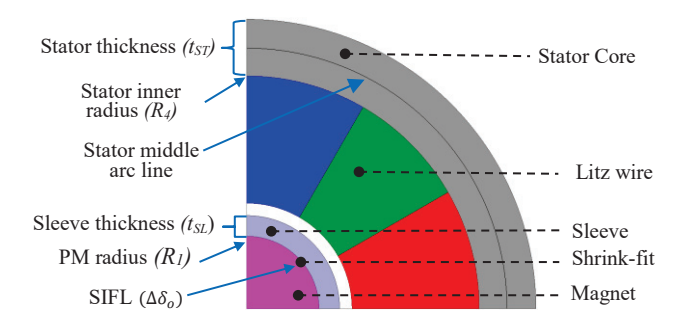


Fig. 6. 2-D parametric FEA electromagnetic model (1/4th) of HP-UHSM.

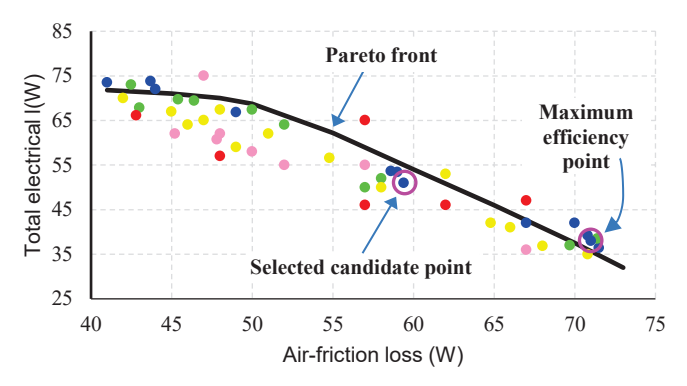


Fig. 7. Trade-off plot and Pareto-front line of the optimization results.

TABLE I
INPUT AND OUTPUT PARAMETERS OF THE OPTIMAL CANDIDATE POINT

Input and obtained parameters	Lower bound	Upper bound	Optimal value	Output parameters	Optimal Value
PM radius $(R_I)$ [mm]	2.5	5	3.9	$B_{st}[T]$	0.61
Sleeve thickness $(t_{SL})$ [mm]	0.25	2	0.7	$J_{den}$ [A/mm <sup>2</sup> ]	4.92
Stator thickness ( $t_{ST}$ ) [mm]	1.5	3.5	2.75	$P_{den}[kW/L]$	64.96
SIFL $(\Delta \delta_o)$ [µm]	5	50	20	$T_{PM}[^{\circ}C]$	124.6
Stack length $(L)$ [mm]	30	60	40	$T_W[^{\circ}C]$	110.2
Phase current $(I_{rms})$ [A]	2.5	10	3.9	$\sigma_{r,PM}[\text{MPa}]$	83.3
Number of turns (Nc)	10	40	20	$\sigma_{t,SL}[\text{MPa}]$	621.2
Number of phases (m)	3	9	6	$P_c$ [MPa]	80.62
Stator in. radius $(R_4)$ [mm]	8	15	11.25	$\omega_{1st}$ [Hz]	9103

#### C. Optimization Results

The optimization is performed using the multi-objective genetic algorithm (MOGA). It is a guided random searchedbased optimization technique, very effective for motor design optimization with multiple objectives and many design variables. Eight design variables are considered in this design. The upper and lower bounds of these variables are given in Table-I. The optimization is converged after 1154 iterations with a six-phase winding configuration,  $Sm_2Co_{17}$  as PM material, titanium alloy as sleeve material, and Amorphous iron as stator material. Fig. 7 shows the trade-off plot obtained by post-processing the optimization results. It has five Pareto-sets (optimal solutions), and the best to worst feasibility goes from blue to red. The best candidate is the one that satisfies all the design constraints and has the maximum DSM considering multi-physics performance. A Pareto-front (optimal-limit line) is drawn manually in Fig. 7. It shows that the total electrical loss and the air-friction loss conflict in an inverse hyperbola manner. It is also observed that the DP at which the total loss is minimum does not have the highest DSM. It has the maximum efficiency of 94.65%, but a DSM of 16% only, considering

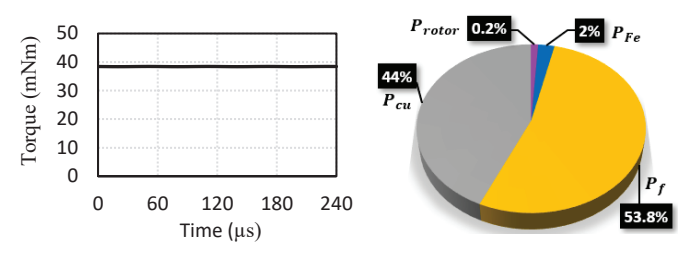


Fig. 8. Electromagnetic torque and loss distribution at rated condition.

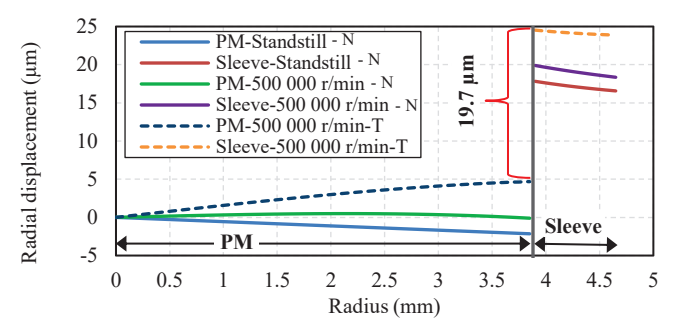


Fig. 9. Radial displacement of AMEBA rotor (N = 25 °C & T = 130 °C).

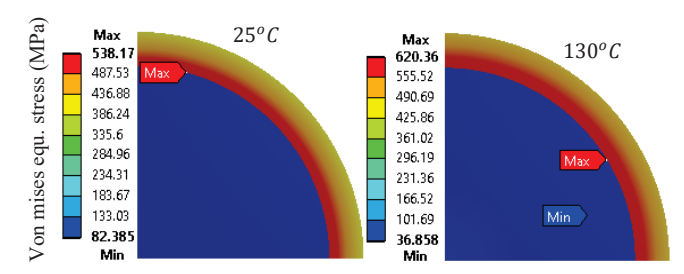


Fig. 10. Stress distribution of AMEBA rotor: (L) 0 r/min, (R) 500 k r/min.

thermal and structural aspects. Hence, instead of using a total loss minimization, the optimal DP is selected by a tradeoff between the two losses and close to the Pareto-front line. The output performances of the optimal DP are also given in Table-I. It satisfies all the specifications and design constraints of the AMEBA rotor and has a 30% DSM with 94.5% efficiency.

# VI. FEA ANALYSIS OF HP-UHS AMEBA ROTOR

# A. Electromagnetic Analysis

The full machine is simulated using a motoring operation. A 6-phase asymmetric toroidal winding with a displacement angle of 30° is implemented in the stator. Each phase has 40 turns in series. The PM and coil temperature are applied as 125° C, and 110° C. Fig. 8 shows that the machine develops an average torque of 38.24 mNm at 500 000 r/min with a sinusoidal current of 3.9 A (RMS). The torque ripple is less than 0.1% due to slotless stator and multi-phase winding. It has a torque constant of 9.8 mNm/A and a back-EMF constant of 2.5×10<sup>-4</sup> V per r/min. The total loss distribution is shown in Fig. 8. It has 94.5% efficiency considering the electrical and air-friction losses. The maximum air-gap flux density is 0.43 T. Therefore, the design UHS rotor satisfies the power requirement of the AMEBA system.

# B. Mechanical Integrity Analysis

The radial displacement of the AMEBA rotor is shown in Fig. 9. At a standstill, the PM is compressed by 2.5  $\mu$ m due to the interference-fitting. At 500 000 r/min, the maximum expansion

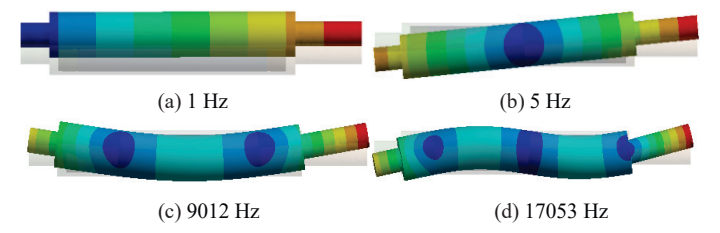


Fig. 11. Deformation modes of the AMEBA rotor at first four UNFs.

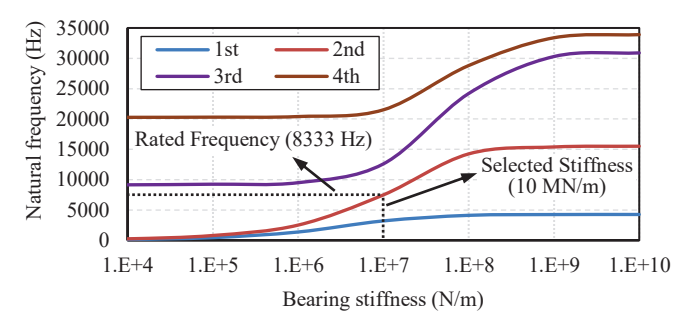


Fig. 12. Natural frequencies vs bearing stiffness of AMEBA rotor.

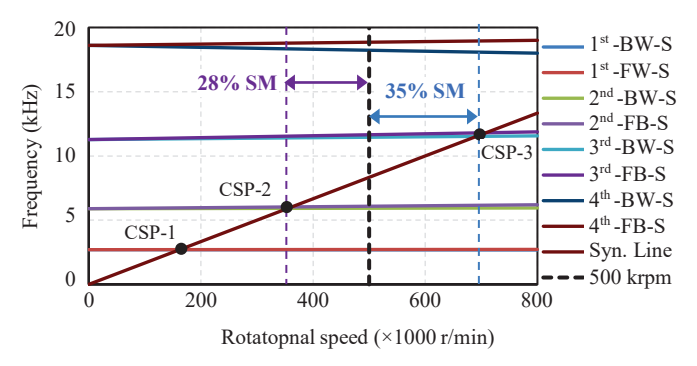


Fig. 13. Campbell diagram of AMEBA rotor. [ S - stable, US – unstable] (CSP = Intersection of natural frequency and synchronous line).

of PM and sleeve outer radius is ~5  $\mu m$  and ~24  $\mu m$ , respectively. It is also shown that operating temperature causes a noticeable rotor displacement. But, due to the similar CTE of PM ( $\alpha_{th}$ = 10) and sleeve ( $\alpha_{th}$ = 9) material, the resultant interference-fit length remains ~19.7  $\mu m$  at 500 000 r/min, ensuring torque transfer.

Fig. 10 shows the stress distribution of the AMEBA rotor. At a standstill, the rotor experiences compressive stress of 82 MPa throughout the entire magnet, and it is equivalent to the static contact pressure. At 500 000 r/min, the maximum von-mises stress occurs at the sleeve inner edge ~620 MPa (65% of titanium limit), and the tensile stress in the PM origin is ~83 MPa (70% of PM limit). At this condition, the contact pressure is 68 MPa, ensuring stable torque transfer. Therefore, the designed rotor has a 30% structural safety margin at 500 000 r/min operation.

# C. Modal Analysis

First, a modal simulation is performed using 3-D FEA under a free-free boundary condition to estimate the AMEBA rotor's UNFs. Fig. 11 shows the first four UNFs and their deformation mode shapes. The first two lower frequencies are rigid body frequencies, generating a lateral (1 Hz) mode shape and a conical (5 Hz) mode shape. The third and fourth frequencies cause the 1<sup>st</sup> order bending mode (9012 Hz) and 2<sup>nd</sup> order bending (17053 Hz) shape. Therefore, it is confirmed that the AMEBA rotor does not have any CBF below 8333 Hz.

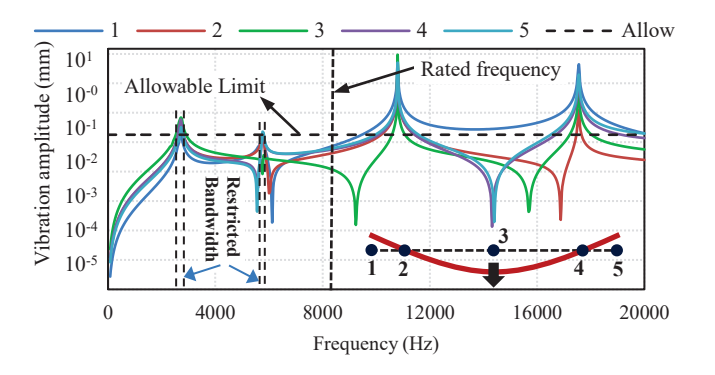


Fig. 14. Unbalance response analysis result of the AMEBA rotor.

Second, the appropriate guide-bearing is selected using the natural frequency vs. bearing stiffness analysis, as shown in Fig. 12. A pair of ball bearings is chosen with a radial stiffness of 10 MN/m. A Campbell diagram of the AMEBA rotor is then obtained by considering the "as installed" boundary conditions, bearing stiffness, and gyroscopic effect to calculate the critical speed points (CSPs). It is highly recommended for any UHS rotor to have at least a 20 to 30% separation margin (SM) between the rotor's CSP and the rated frequency [18]. In Fig. 13, it is observed that the two rigid body modes are moved from 1 Hz to 2806 Hz and 5 Hz to 5956 Hz due to the bearing stiffness. Also, the bending frequencies are shifted from 9012 Hz to 11250 Hz and 17053 Hz to 21003 Hz. As a result, the rated speed point (RSP) falls between the 2<sup>nd</sup> and 3<sup>rd</sup> CSP. However, there is a 28% SM between the RSP and 2<sup>nd</sup> CSP; and 35% SM considering the 3<sup>rd</sup> CSP. Fig. 13 also shows, as the rotational speed increases, each natural frequency is split into a forward whirl (FW) mode and a backward whirl (BW) mode due to the gyroscopic effect. For the AMEBA rotor, all these modes are stable, and the difference between FW and BW modes of the CPSs is negligible, confirming excellent rotor stability at UHS.

# D. Unbalance Response Analysis

Unbalance harmonic force at critical resonances is one of the major vibration sources of the UHS rotating shaft. An unbalance harmonic response analysis is performed to investigate the vibration amplitude, air-gap clearance, and the restricted frequency bandwidth of the AMEBA rotor due to its unbalance characteristics. For the designed rotor, the permissible residual unbalance can be calculated by ISO standard-1940 [19] as (17):

$$U_{max} = 1000 \left(\frac{G \times M}{N}\right)$$
 g.mm (17)

where G is the balance quality grade, which is 0.4 mm/s for the UHS rotor, M is the rotor mass (kg), and N is the rotating speed (rad/s). The calculated unbalance mass is applied on the rotor center, considering the 1<sup>st</sup> order bending mode, as shown in Fig. 14. It also shows the frequency response function (FRF) result of unbalanced response analysis at different rotor points. The acceptable vibration amplitude ( $V_{allow}$ ) of the proposed rotor can be roughly calculated using the API standard-610 [20] as (18):

$$V_{allow} = 25.4\sqrt{\left(\frac{12000}{N}\right)}$$
 (18)

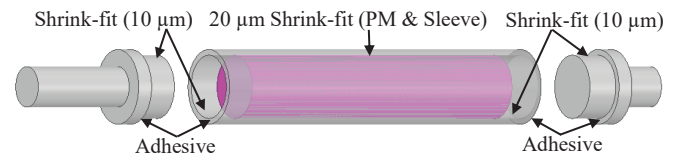


Fig. 15. The AMEBA rotor development using the shrink-fit technique.



Fig. 16. (a) UHS ball bearing, (b) sleeve, (c) shaft parts, (d) cylinderical magnet, (e) assembeled rotor, (f) insulated stator with 6-phase toroidal winding, and (g) final HP-UHSM prototype with aluminium casing.

Fig. 14 shows that, at 8333 Hz, both the vibration amplitude and the air-gap clearance are well below the allowable limit (12.2 μm and 0.54 mm, respectively). However, at the 3<sup>rd</sup> and 4<sup>th</sup> critical frequencies, the vibration amplitude exceeds the acceptable limit severely, and the rotor fails to maintain the minimum clearance in the air-gap. Therefore, this AMEBA rotor should never pass these critical frequencies to avoid catastrophic failure. It is also observed that the vibration level at the 1<sup>st</sup> and 2<sup>nd</sup> CSPs reach the allowable limit, but their corresponding restricted frequency bandwidths are very small. It is 2798 Hz to 2982 Hz for 1<sup>st</sup> order critical resonance and 5949 Hz to 5993 Hz for 2<sup>nd</sup> order critical resonance. These bandwidths are small but should pass quickly and carefully.

# VII. PROTOTYPING AND EXPERIMENTAL VALIDATION

### A. Prototype Development

The proposed AMEBA rotor is built using the shrink-fit technique, as shown in Fig. 15 and 16. The titanium parts are designed using CNC machining with a tolerance precision of ± 0.005 mm. The cylindrical PM  $(Sm_2Co_{17})$  is diametrically magnetized. The sleeve was heated up to 340° C using an induction heater, and the PM was cooled down to -190° C using the liquid nitrogen (LN) to obtain a 20 µm interference-fit between them. Attention must be taken during this fitting so as not to have any LN frost on the magnet surface to avoid corrosion. Shaft parts are installed using adhesive and shrinkfit technique, as shown in Fig. 15. The adhesive is used in the joint of the shaft part and sleeve to improve the bonding. A pair of customized UHS ball bearings are used, which can operate at 500 000 r/min continuously for at least 15 hours. In the stator, a 6-phase asymmetric (30-degree phase displacement between two 3-phase sets) toroidal winding is applied on the Metglas-2605SA1 core, as shown in Fig. 16 (f). Each phase has 40 turns in series, and each turn has 100 strands of 40-AWG Litz wire. The full motor with an aluminum casing is shown in Fig. 16 (g).

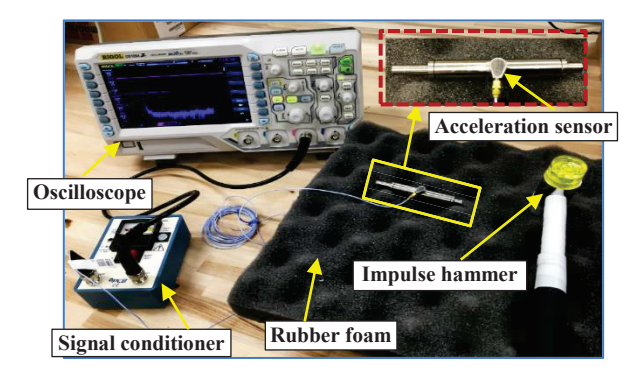


Fig. 17. Impact hammer test setup of AMEBA rotor prototype.

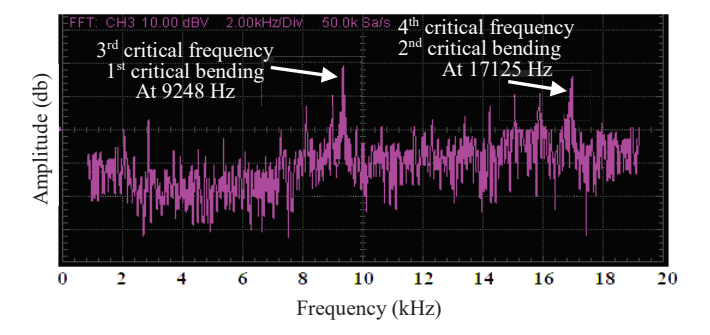


Fig. 18. Frequency spectrum result of the impulse hammer test.

# B. Impulse Hammer Testing

An impulse hammer test is performed to validate the CBFs of the FEA results. Fig. 17 shows the test setup, where a tip changeable impulse hammer is used to excite the rotor mechanically, and an IEPE acceleration sensor is used to measure the rotor's frequency response. A signal-conditioner is used to power the sensor and to amplify the sensor output. The sensor is attached to the rotor surface, and a low attenuating non-stiff media supports the rotor to ensure the undamped freefree boundary condition. Two testing methods (roving hammer method and roving sensor) are performed. In each case, different hammer tips are used and found very similar results. Fig. 18 shows the FRF result of the proposed rotor when it is mechanically excited by the impulse hammer. In the plot, the first two rigid body modes are not separable due to their low amplitude. However, two separable peaks are visible in the spectrum at 9248 Hz and 17125 Hz, which are the 1st and 2nd order bending modes, respectively. The test results have an excellent agreement with the FEA results of Fig. 10 with an error of 1.6%, which is acceptable. The mechanical excitation is kept limited to ~20 kHz to avoid PM mechanical breakdown.

# C. Electromagnetic and Structural Testing

First, the no-load back-EMF is measured of the rotor using a motor-generator operation. Fig. 19 shows the phase-A back-EMF of the prototype at 50 000 r/min. The experimental result has a back-EMF constant of  $2.5 \times 10^{-4}$  V per r/min, which closely agrees with the FEA result. Then, a variable resistor is connected to the UHSM and measured the reaction torque using  $T_e = 1.5 m i_r \Psi_{pm}$ , where  $\Psi_{pm}$  is the PM flux linkage calculated from back-EMF information and  $i_r$  is the peak current through the external resistor. The calculated torque and measured torque are presented in Table II, which gives a torque constant of  $\sim 9.8$ 

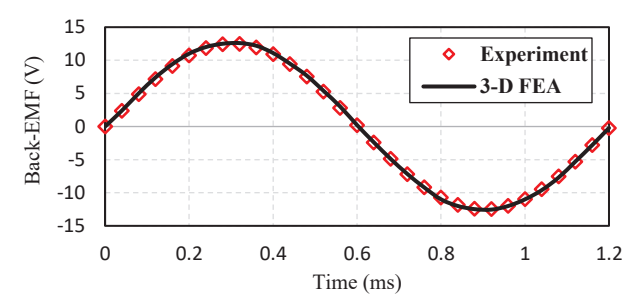


Fig. 19. No load back-EMF (Ph-A) of the rotor prototype at 50 000 r/min.

# TABLE II COMPARISON OF PREDICTED AND MEASURED TORQUE VS PHASE CURRENT

Phase current (RMS)	0.5 A	1 A	1.5 A	2 A	2.5 A	3 A
Calculated torque (mNm)	4.9	9.8	14.7	19.6	24.5	29.4
Measured torque (mNm)	4.94	9.86	14.75	19.64	14.52	29.43

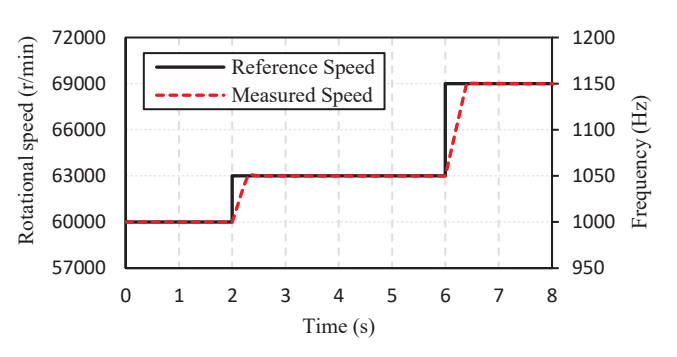


Fig. 20. Rotor dynamic test using reference speed tracking

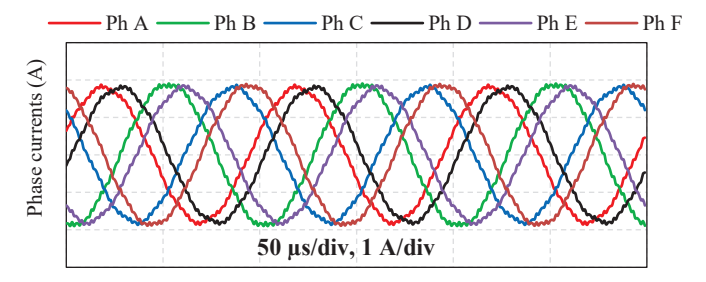


Fig. 21. Measured six-phase stator current at 60 000 r/min.

mNm/A. The reaction torque is measured at low speed, so the air-friction and eddy current losses are neglected. Finally, the machine is operated at UHS using the no-load motoring operation to validate the rotor's structural integrity. Therefore, the rotor's electromagnetic properties match very well with the FEA results.

# D. Dynamic Testing

The dynamic operation of the prototyped rotor is tested at a lower speed and no-load condition. Initially, the machine is operated at 1000 Hz. Then a step command of 50 Hz and 100 Hz are applied in the reference speed at 2 seconds and 6 seconds, respectively, as shown in Fig. 20. This scenario realizes the AMEBA system's dynamic operation similar to Fig. 2 at the ULF condition. It is observed that the measured rotor speed tracks the step commands less than 0.5 second, resulting in a dynamic of ~200 Hz/s. Note that the rotor is designed to perform 12 Hz/s at the rated condition, which is well below the 200 Hz/s. Fig. 21 shows the six-phase stator input current at 60

000 r/min. The cylindrical PM and slot-less stator produce a sinusoidal current with some higher-order harmonics due to switching frequency.

#### VIII. CONCLUSION

A new multi-physics design approach of the HP-UHS rotor for AMEBA application is presented in this paper. The design method includes the electromagnetic, thermal, structural, and rotordynamic analysis to consider the multi-disciplinary critical design constraints of the AMEBA rotor and their mutual influences. The DOE and kriging method-based approximation models are used in the optimization to effectively address the nonlinearities of the AMEBA rotor. Multiple objective functions and Pareto-front analysis are adopted to obtain an efficient design with high DSM. By using the developed design method, a 2 kW 500 000 r/min UHSM is optimized explicitly for a ULF-VLF AMEBA system. The optimization is performed using the MOGA, and the optimal DP is obtained by a trade-off between the efficiency and DSM. The detailed FEA is performed to investigate the mechanical integrity, resonance frequency, and vibration of the AMEBA rotor. Finally, the rotor is prototyped and tested for AMEBA system requirements. The proposed rotor has 38.2 mNm rated torque, 94.5% efficiency, 30% DSM, and no CBF below 8.5 kHz. These multidisciplinary benefits make the rotor suitable for the AMEBA system by ensuring a stable, wide bandwidth, and efficient field generation capability. Furthermore, its miniature size makes the AMEBA transmitter compact and portable. In future work, a UHS test bench will be developed, and the proposed AMEBA rotor will be studied for the AMEBA's communication operation up to 8.3 kHz using the PPM as a load.

### **ACKNOWLEDGMENT**

This research was supported in part by the NSF CCSS-Comms Circuits & Sens System Program (Award # 1905434).

# REFERENCES

- D. Gerada, A. Mebarki, N. L. Brown, C. Gerada, A. Cavagnino and A. Boglietti, "High-Speed Electrical Machines: Technologies, Trends, and Developments," IEEE *Trans. on Ind. Electron.*, vol. 61, no. 6, pp. 2946-2959, June 2014.
- [2] Z. Huang and J. Fang, "Multiphysics Design and Optimization of High Speed Permanent-Magnet Electrical Machines for Air Blower Applications," IEEE *Trans. on Ind. Electron.*, vol. 63, no. 5, pp. 2766-2774, May 2016
- [3] P. Pfister and Y. Perriard, "Very-High-Speed Slotless Permanent-Magnet Motors: Analytical Modeling, Optimization, Design, and Torque Measurement Methods," IEEE *Trans. on Ind. Electron.*, vol. 57, no. 1, pp. 296-303, Jan. 2010.
- [4] M N, S.P., Tok, R.U., Fereidoony, F. et al. Magnetic Pendulum Arrays for Efficient ULF Transmission. Sci Rep 9, 13220 (2019).
- [5] S. Gong, Y. Liu, and Y. Liu, "A Rotating-Magnet Based Mechanical Antenna (RMBMA) for ELF-ULF Wireless Communication," *Progress In Electromagnetics Research M*, Vol. 72, 125-133, 2018.
- [6] J. S. Glickstein, J. Liang, S. Choi, A. Madanayake and S. Mandal, "Power-Efficient ELF Wireless Communications Using Electro-Mechanical Transmitters," *IEEE Access*, vol. 8, pp. 2455-2471, 2020.
- [7] J. D. Ede, Z. Q. Zhu and D. Howe, "Rotor resonances of high-speed permanent-magnet brushless machines," *IEEE Trans. on Ind. Appl.*, vol. 38, no. 6, pp. 1542-1548, Nov.-Dec. 2002.
- [8] D. Hong, B. Woo and D. Koo, "Rotordynamics of 120 000 r/min 15 kW Ultra High Speed Motor," *IEEE Transactions on Magnetics*, vol. 45, no. 6, pp. 2831-2834, June 2009.
- [9] C. Zwyssig, J. Kolar, W. Thaler and M. Vohrer, "Design of a 100 W 500000 rpm permanent-magnet generator for mesoscale gas turbines", Fourtieth IAS Annual Meeting. Conference Record of the 2005 Industry Applications Conference 2005, pp. 253-260, 2005.

- [10] C. Zwyssig, S. D. Round, and J.W. Kolar, "An ultrahigh-speed, low power electrical drive system," *IEEE Trans. on Ind. Electron.*, vol. 55, no. 2, pp. 577–585, Feb. 2008.
- [11] F. R. Ismagilov, N. Uzhegov, V. E. Vavilov, V. I. Bekuzin and V. V. Ayguzina, "Multidisciplinary Design of Ultra-High-Speed Electrical Machines," *IEEE Trans. on Energy Convers.*, vol. 33, no. 3, pp. 1203-1212, Sept. 2018.
- [12] C. Gong, S. Li and T. Habetler, "High-Strength Rotor Design for Ultra-High Speed Switched Reluctance Machines," *IEEE Trans. on Ind. Appl.*, vol. 56, no. 2, pp. 1432-1442, March-April 2020.
- [13] A. Borisavljevic, H. Polinder and J. A. Ferreira, "On the Speed Limits of Permanent-Magnet Machines," in *IEEE Trans. on Ind. Electron.*, vol. 57, no. 1, pp. 220-227, Jan. 2010,
- [14] G. Du, W. Xu, J. Zhu and N. Huang, "Effects of Design Parameters on the Multiphysics Performance of High-Speed Permanent Magnet Machines," *IEEE Trans. on Ind. Electron.*, vol. 67, no. 5, pp. 3472-3483, May 2020,
- [15] J. D. Hartog, "Mechanical vibrations," New York: McGraw-Hall Book Company, 1947.
- [16] S. Timoshenko and J. Goodier, Theory of elasticity. New York, USA: McGraw-Hill, 1970.
- [17] X. Sun, Z. Shi, G. Lei, Y. Guo and J. Zhu, "Multi-Objective Design Optimization of an IPMSM Based on Multilevel Strategy," *IEEE Trans.* on Ind. Electron., vol.68, no.1, pp.139-148, Jan.2021
- [18] Hong, Do-Kwan et al. "Unbalance response analysis and experimental validation of an ultra-high-speed motor-generator for microturbine generators considering balancing." Sensors, vol.14,9 16117-27. Aug. 2014
- [19] ISO 1940-1, Mechanical vibration balance quality requirements of rigid rotors part 1: determination of permissible residual unbalance.
- [20] API Standard 611, General-purpose steam turbines for petroleum, chemical, and gas industry services, 5<sup>th</sup> edition, Washington, D.C. (2004).



Md Khurshedul Islam (S'20) received a B.S. degree in Electrical and Electronic Engineering from International Islamic University Chittagong (IIUC) in 2014. From 2014 to 2017, he worked as a Lecturer at IIUC, Bangladesh. He is currently pursuing a Ph.D. degree with the Mississippi State University, Starkville, MS, USA, from 2017. His research interests are electric motor design, motor control, PM motor, Multiphysics analysis, and high-speed drive.



**Seungdeog Choi** (S'07–M'12–SM'16) received the B.S. degree from Chung-Ang University, Seoul, South Korea, in 2004, the M.S. degree from Seoul National University, Seoul, in 2006, and the Ph.D. degree in electric power and power electronics program from Texas A&M University, College Station, TX, USA, in 2010. He has been an Associate Professor with Mississippi State University, Starkville, MS, USA, since 2018. His current research interests include the degradation modeling, fault-tolerant

controls, fault-tolerant design, and EMI analysis of electric machine, power electronics in the transportation application.



Yang-Ki Hong received the B.S. degree in physics and the M.S. degree in solid-state physics (magnetism) from Yonsei University, Seoul, South Korea, in 1972 and 1974, respectively, and the Ph.D. degree in metallurgy from the University of Utah, Salt Lake City, UT, USA, in 1981. He is currently the E.A. "Larry" Drummond Endowed Chair Professor with the Department of Electrical and Computer Engineering and a Professor of materials science Ph.D. Program with The University of Alabama, Tuscaloosa, AL, USA. His current research interests

include magnetism, electromagnetics, magnetic materials, and RF devices.



Sangshin Kwak (Member, IEEE) received his Ph.D. degree in electrical engineering from Texas A&M University, College Station, TX, USA, in 2005. From 2007 to 2010, he was an Assistant Professor with Daegu University, Gyeongsan, South Korea. Since 2010, he has been working with Chung-Ang University, Seoul, South Korea, where he is currently a Professor. His research interests include the design, modeling, control, and analysis of power converters for electric vehicles, and renewable energy systems as well

as the prognosis and fault tolerant control of power electronics systems.